# THE CIMR SATELLITE – CHALLENGES AND SOLUTIONS FOR AOCS DESIGN

**F. Santilli [(1),a], A. Primavera [(1),b], F. Santoni [(1),c], G. Zaccari [(1),d], F. Gennari [(1),e], A. Colella [(1),f], M. Ficorilli [(1),g], A. Kornienko [(2),h], A. Hyslop [(2),i], M. Triggianese [(2),l], M. Sallusti [(2),m]**

*[(1)] Thales Alenia Space Italy (TAS-I), Via Saccomuro 24, 00131 Rome, Italy*
*{ [(a)]email: francesco.santilli@thalesaleniaspace.com*
*[(b)] email: asia.primavera@thalesaleniaspace.com*
*[(c)]email: francesco.santoni@thalesaleniaspace.com*
*[(d)]email: giulia.zaccari@thalesaleniaspace.com*
*[(e)]email: fabrizio.gennari@thalesaleniaspace.com*
*[(f)]email: Antimo.colella-somministrato@thalesaleniaspace.com*
*[(g)]email: marco.ficorilli@crat.eu }*
*[(2)]European Space Agency (ESA - ESTEC),* 2201 AZ Noordwijk, Netherlands
*{[(h)]email: andrey.kornienko@esa.int*
*[(i)]email: andrew.hyslop@esa.int*
*[(l)]email: mariel.triggianese@esa.int*
*[(m)]email: marcello.sallusti@esa.int}*

## ABSTRACT

Ocean warming, sea level rise and ice melting caused by climate change have serious consequences for the global economy, navigation and security. CIMR stands for Copernicus Imaging Microwave Radiometer and it is a Copernicus Expansion mission [1] answering to the EU Artic policy [2]. CIMR project is implemented by the European Space Agency (ESA) and the European Commission (COM), it is currently in the C/D phase with Thales Alenia Space as prime contractor. The two CIMR satellites use a conically scanning microwave radiometer capable of providing high global resolution images of floating artic sea ice parameters across various frequency bands. In order to maintain a wide ground swath, the satellite instrument rotates continuously around a local vertical axis. From an AOCS standpoint, the unique configuration consisting of the 3-axis stabilized platform and the spinning instrument are quite challenging. The paper presents an overview of the CIMR AOCS design and its main design drivers, together with the major challenges. Special features of CIMR AOCS design are: the on-board estimation of static and dynamic unbalances using gyro rate measurements and compensation through active balancing system; management of the large angular momentum induced by the instrument rotating part through momentum exchange units on the platform; the on-board control laws that guarantee an overall systems stability and robustness in presence of undesired coupling caused by internal disturbances, flexible dynamics, and time-varying uncertainties; the controlled re-entry manoeuvers through multiple apogee thruster firings in presence of critical drag at perigee passages.

## 1 INTRODUCTION

The Copernicus Imaging Microwave Radiometer mission, namely CIMR mission, will guarantee improved continuity of missions monitoring the Polar Regions in terms of measurement bands, spatial resolution, temporal resolution and geophysical accuracy in support of Copernicus Services.

The following primary objectives have been established for the mission [3]:

- Measure Sea Ice Concentration (SIC) and Sea Ice Extent (SIE) at a spatial resolution of ≤ 5 km, with a standard uncertainty of ≤ 5%, and sub-daily coverage of the Polar Regions and daily coverage of Adjacent Seas;
- Measure Sea Surface Temperature (SST) at an effective spatial resolution of ≤ 15 km, with a standard uncertainty of ≤ 0.3 K and focusing on sub-daily coverage of Polar Regions and daily coverage of Adjacent Seas.

In order to fulfil its mission and achieve the footprint requirements (shown in Figure 1), the spacecraft will embark a conically-scanning passive imaging microwave radiometer payload and will operate across five spectral bands (L/C/X/Ku/Ka), corresponding to frequencies of 1.4, 6.9, 10.65, 18.7, and 36.5 GHz. One of the key features of CIMR mission is the polarized measurements in low frequency channels at relatively high resolution compared to other microwave radiometer missions (e.g. SMAP mission).

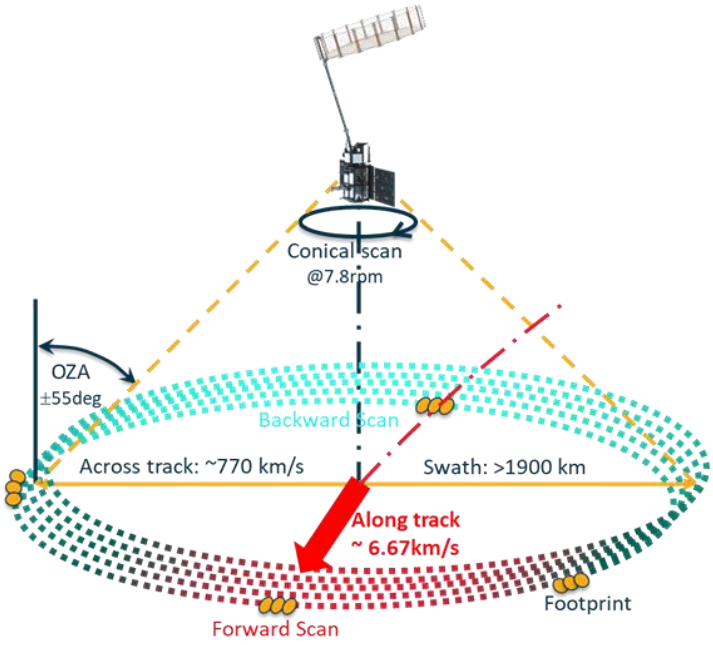


Figure 1. CIMR imaging concept.

## 1.1 Mission Analysis

CIMR reference orbit is sun-synchronous dawn/dusk, having a frozen eccentricity and an average altitude of around 817 km. The value of semi-major axis is such that the ground track is repeatable, with an orbital cycle duration of 29 days. The spacecraft has a nominal lifetime of 7.5 years, with a possible extension of 5 additional years, and it is designed to be compatible with a launch with VEGA-C from Kourou, considering Ariane 6 as back-up launcher.

During its operational life, CIMR satellite has to maintain its ground track with respect to the nominal one of MetOp-SG(B) [4], in particular within ±5 km at the equator and ±2 km at the poles, in order to ensure good co-located data from both missions.

In a LEO, the most important perturbations that have an impact on the nominal orbit are the atmospheric drag and the third body effects due to the Sun and the Moon. In particular, the major effect of the atmospheric drag is an orbit altitude decay which is compensated by in-plane

manoeuvres, while Sun and Moon gravitational attractions produce a movement of the orbital plane that is compensated by out-of-plane manoeuvres.

In-plane manoeuvres are performed in order to comply with the requirement regarding the ground track maintenance at the equator, more precisely by controlling the shift in longitude of the orbital nodes. The frequency of in-plane manoeuvres and the delta-V related to each of them depend on the solar activity that the satellite encounters along its lifetime.

Out-of-plane manoeuvres are instead performed in order to guarantee the ground track maintenance at the poles, correcting the variation of orbital inclination, but they also have the aim of keeping the mean local time of the ascending node around its nominal value.

Once the operational life is over, the satellite has to be deorbited, and specifically for CIMR a controlled re-entry is planned. Performing a controlled re-entry is the most efficient way to proceed with regard to lifetime reduction and human casualty risk control, as it foresees a predetermined point of impact in the SPOUA (South Pacific Ocean Uninhabited Area). However, it implies tougher constraints for the spacecraft which consequently increases the complexity of the entire mission. Whereas the duration of the first manoeuvres can be arbitrarily decided by making a trade-off between firing efficiency and number of manoeuvres to be implemented, the duration of the last burn is strictly related to the minimum perigee altitude reachable by the satellite, and it is inevitably longer than the one of the preceding manoeuvres. In particular, the minimum reachable perigee altitude depends on the satellite's ability to counteract the disturbance torques.

## 1.2 Satellite description

### 1.2.1 CIMR Layout Description

The space segment of the mission is made up of a three-axis stabilized platform (PLF), whose mean pointing direction is always directed along the local vertical, and an instrument rotating part that will carry a Large Deployable Reflector system (LDRS). The rotating part spins at a constant rate of 7.8 rpm with respect to the platform by means of a scan mechanism (SCM). The deployable mesh reflector has a diameter of 8 meters and a feed cluster, which produces a 1900 km wide ground swath due to the rotation. The deployment of the eight meters mesh antenna is comprised of two main events: the release and deployment of the multi-segment hinged boom assembly, and the release and deployment of the perimeter truss antenna itself.

For the AOCS design, CIMR layout is modelled by a series of bodies and geometric objects. Each of them is associated with a unique reference frame and is attached to a parent body through a joint, while multiple geometric objects can be defined as part of a body. For analysis purposes, two different layouts are defined: LDR stowed and LDR deployed, both of them showed in Figure 2.

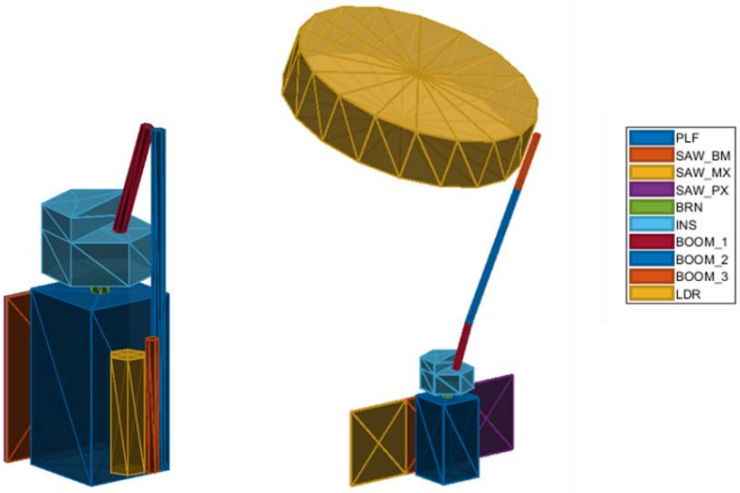


Figure 2. CIMR layout: stowed and deployed configurations.

### 1.2.2 Main Reference Frames

Figure 3 shows the reference frames in the satellite deployed configuration. The main ones are:

- MRF - Spacecraft Mechanical Reference Frame (MRF) is a right-handed frame with the origin $O_S$ located at the center of the satellite separation plane between spacecraft and launcher, $Z_S$ defined as the direction orthogonal to that plane and $Y_S$ defined in the separation plane with the direction orthogonal to solar array body mounted panel;
- LOF - Local Orbital Reference Frame ($X_{orb}$, $Y_{orb}$, $Z_{orb}$) has the origin in the center of mass of the satellite, $Z_{orb}$ with the same direction of the satellite center of mass position vector from the Earth center and $Y_{orb}$ perpendicular to the current orbital plane and in the same direction of the current orbital momentum. $X_{orb}$ belongs to the orbital plane with a positive projection onto the satellite velocity;
- Geodetic Zero-Doppler Reference Frame is similar to the LOF, but with Z along the local vertical of the Earth surface and X toward the satellite velocity in ECEF (Earth Centered Earth Fixed);
- IF - Instrument Interface Reference Frame ($X_{IF}$, $Y_{IF}$, $Z_{IF}$) is a frame fixed to the body, where the origin is the intersection point between the instrument interface plane with the platform and the instrument rotation axis, and the three axes oriented as the MRF;
- INS - Instrument Spun Reference Frame ($X_{INS}$, $Y_{INS}$, $Z_{INS}$) is jointed to the instrument rotating part, thus rotating around $Z_{INS}$. The origin is in the intersection point between the interface plane of the instrument rotating part with the SCM and the instrument rotation axis, $+X_{INS}$ axis is oriented so that the $-X_{INS}$ axis crosses the LDRS boom attachment side.

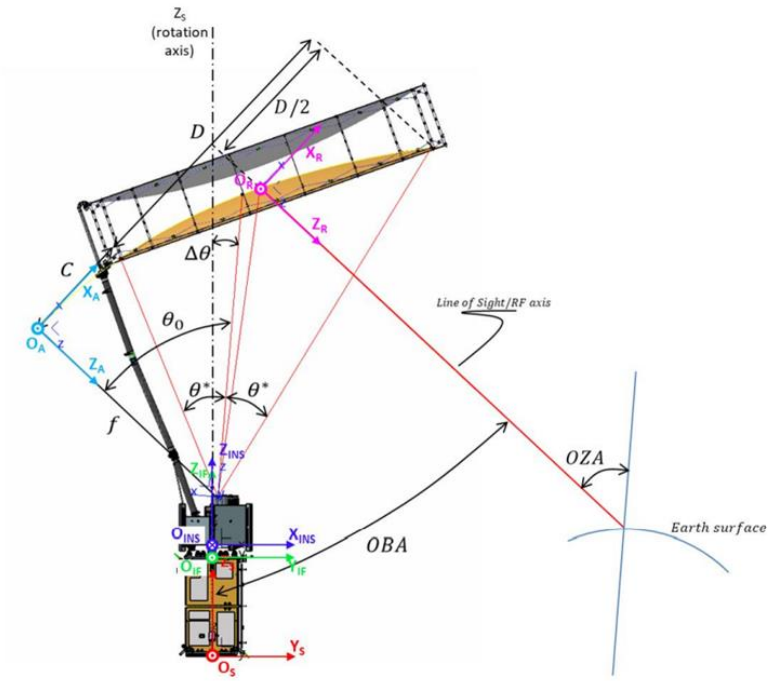


Figure 3. CIMR reference frames in the fully deployed configuration.

## 2 AOCS DESIGN DRIVERS

The AOCS design is significantly driven by the spacecraft configuration where the payload with high rotational inertia is spinning relatively to the 3-axis stabilized platform. Along with considerations at system level this setup poses significant challenges for the AOCS design.
Figure 4 gives an overview of the main CIMR AOCS design drivers.

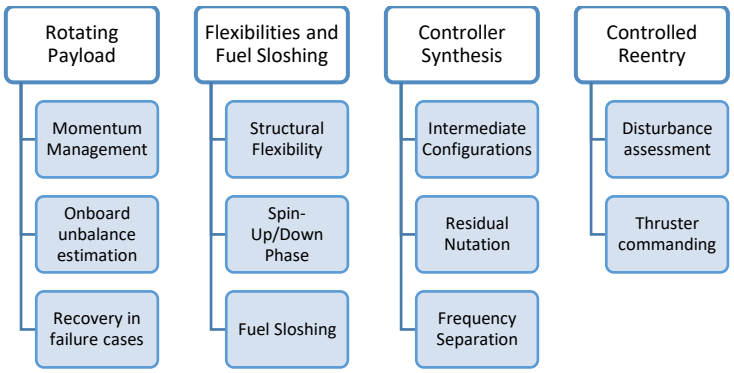


Figure 4. Major AOCS design drivers.

### 2.1 Rotating Payload

The large angular momentum around 1000 Nms induced by the instrument rotating part needs to be compensated by the momentum exchange units on the platform side to ensure the net angular momentum of the entire system close to zero. The AOCS is in charge of the processing chain of the angular momentum management and generating required commands to the momentum compensation wheels.

The spinning instrument is distinguished by the large deployable antenna. Once deployed in-orbit and operated at nominal rotation speed, certain static and dynamic unbalance effects are expected, which contribute to nutation dynamics of the spacecraft and thus to the pointing performance. To mitigate the unbalance effects, the rotating part of the instrument is equipped with a dedicated Active Balancing System (ABS). The AOCS is responsible for the on-board estimation of these unbalances to be periodically compensated by the ABS during commissioning, with ground operation in the loop. More details of the unbalance estimation algorithm is provided in section 4.1.

Due to high angular momentum on the platform and instrument, the AOCS design shall be tolerant to failure cases of different severity and to allow appropriate reconfiguration of the units and fast attitude recovery.

### 2.2 Flexibilities and Fuel Sloshing

The attitude controllers should accommodate for various structural flexibilities of the spacecraft at different operation modes.

On the platform side, the solar array flexibilities and the sloshing effects of the propellant affect the dynamics. In detail, the fuel in the tank rotates in the instrument rotation direction due to the conic motion of the platform, resulting in an additional internal momentum to be compensated.

### 2.3 Controller Synthesis

Beside flexibility and sloshing consideration in the design, the AOCS should deal with a variety of intermediate conditions in the deployment phase and in potential deployment failure cases.

For continuous acquisition of the payload data, the spacecraft's antenna off-zenith angle (OZA) depicted in Figure 1 should be kept within the range [53,57] degrees for C, X, K, and Ka bands, and within the range [51,53] degrees for L band [5]. This gives a break-down of the pointing requirements allocated to AOCS:

- APE: 4.06 mdeg bias and 4.517 mdeg (1σ) variation;
- PDE: 8 mdeg (1σ) drift over one scan instrument rotation period (7.7 sec);
- AKE: 4.06 mdeg bias and 1.585 mdeg (1σ) variation.

In addition, moderate slew manoeuvers along the pitch axis are required for the instrument calibration.

The in-orbit balancing calibration of the rotating payload can be achieved to a certain accuracy limited by the unbalancing estimation knowledge, ABS positioning errors and thermo-elastic effects. Thus, the residual nutation motion shall be considered by the AOCS.

Another challenging design implication is posed by the presence of the scan mechanism controller responsible for the instrument rotation. In order to avoid undesired coupling effects a certain frequency separation should be ensured between the AOCS and scan mechanism controllers as well as the lowest flexible mode.

### 2.4 Controlled Re-Entry

At the end of the nominal lifetime the CIMR spacecraft shall be disposed using series of controlled re-entry manoeuvers for the perigee lowering. Thus the accurate disturbance assessment of the entire re-entry phase is the key driver for appropriate actuator sizing and guidance optimization.

Thruster commanding also plays a crucial role in achieving a controlled re-entry. AOCS shall be able to manage the distribution of thrust force, by maintaining attitude control during the perigee lowering phase.

# 3 AOCS DESIGN OVERVIEW

## 3.1 Avionics architecture

The avionics of the CIMR satellite is composed by the following equipments shown in Figure 5:

- On Board Computer (SMU-NG) - includes also the GNSS receiver;
- RTU - handles acquisition and generation of analogue signals;
- 3 Magneto-bars (MTB) - for wheels desaturation and safe mode control (400 $Am^2$);
- 2 Magnetometers (MAG) - for safe mode control;
- 8 Cosine Sun Sensors (CoSS) - for safe mode control;
- 4 Reaction Wheels (RWS) – For attitude control in nominal mode and momentum bias in safe mode (0.2 Nm, 50 Nms);
- 5 Momentum Compensation Wheels (MCW) – For instrument momentum compensation (0.12 Nm, 250 Nms);
- 2 Gyroscopes (GYRO) – For attitude control and unbalance estimation;
- 3 Star Trackers (optical heads) – For precise attitude determination. Star fusion is performed by a software provided by the supplier that runs in the on board computer.

In addition, the avionic subsystem is capable of controlling:

- 6 thrusters - 1 N for orbit orbit maintenance manoeuvres and collision avoidance manoeuvres during the satellite operational life;
- 8 thrusters - 20N for rate damping after separation, for the correction of launcher injection errors and for the manoeuvres of the disposal phase.

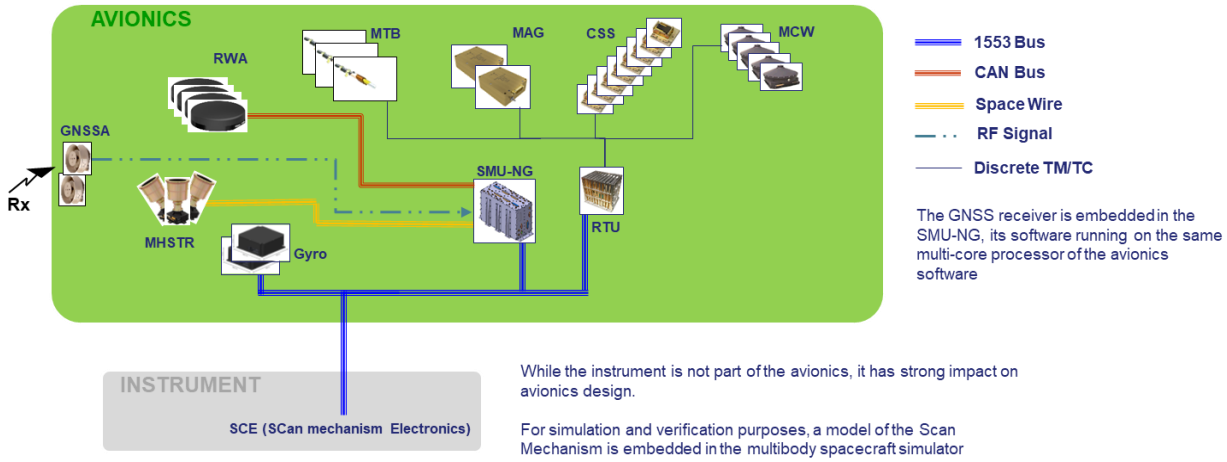


Figure 5. Avionics block diagram.

## 3.2 AOCS modes and transitions

CIMR will feature a relatively complex AOCS mode architecture due to the challenges of different mission phases.

Figure 6 shows the overall CIMR operative modes with their relative transition phases:

- IDLE: no AOCS control, the satellite will be in this mode only at ground, in the launch phase and during software restart;
- SAFE_HRD (High-Rate Damping): is an operative mode featuring thrusters for rate damping; it will be used only at launcher separation, if needed. After deployment, it will be inhibited because the large torques exerted by the thrusters can damage the Scan Mechanism. This mode is transient because it only reduces the satellite angular rate, the sun pointing is guaranteed in SAFE. The rate is measured with the gyroscope;
- SAFE: is the operative mode that guarantees the satellite survival and commandability in case of reconfigurations. It features the phase "RATE" that uses only MTB and MAG to perform control (according to B-DOT law), enabling rate damping but also sun pointing (due to passive stability toward the orbit normal-vector). The second phase "ATT" (attitude) uses also the sun sensors and the gyro to achieve a 3-axis pointing for nominal phase. An on-board orbit propagator with data provided by ground is used to achieve 3-axis pointing;
- SAFE_MOM (Safe Momentum): is dedicated to recover a safe condition in case of failure while the instrument is rotating. It will restore the momentum balancing that might have been lost during software restart, before activating an autonomous transition to the SAFE mode (that will otherwise fail if the instrument momentum is not balanced). It performs an attitude control only on Z-axis (using momentum wheels) to achieve the sun pointing;
- NOM: is the nominal mode of the satellite during the mission. It features a "SLEW" phase for transient during mode transition and manoeuver calibration, along with a "CRUISE" phase to maintain the attitude requested by the mission. The orbital position is obtained from a GNSS receiver and filtered with an internal propagator, and the attitude performances are achieved by means of the gyro and star tracker measurements;
- THRUST_OCM: is used to perform station keeping manoeuvers. The phases (and controller) are the same of the NOM mode, but it features the use of the thrusters and different controller gains and FDIR thresholds;
- THRUST_REM: is used for controlled re-entry. It features different phases to support attitude control by means of thrust commanding while firing, and a dedicated phase to handle the perigee crossing at low altitude (with high drag torque disturbances).

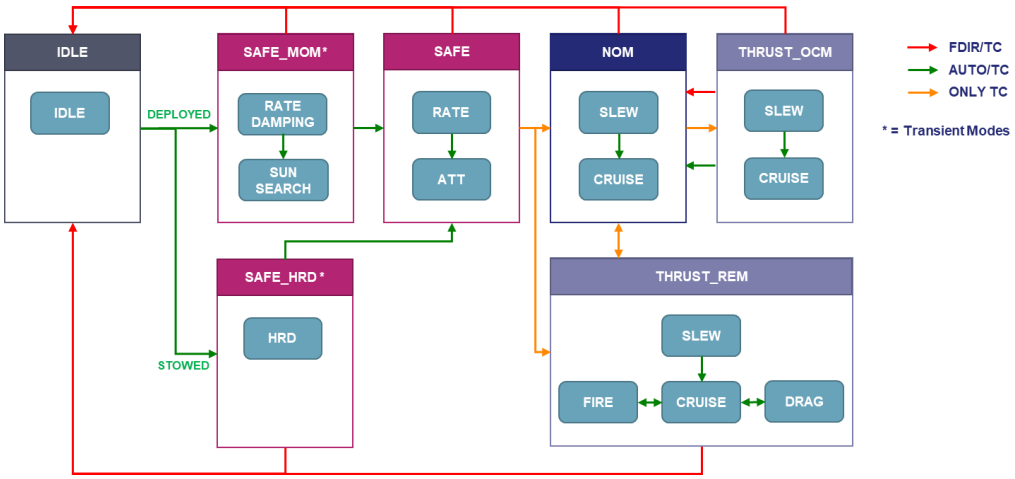


Figure 6. CIMR operative modes and transition phases.

The FDIR (Fault Detection, Isolation and Recovery) for the avionics will be mostly based on online recoveries (in case of failures of units that are redounded) and software restarts (for all other cases such as pointing anomalies and software crash). No autonomous mode transition are foreseen in case of failures; to ensure that the issue is solved in the most safe way, a software restart is triggered to enter the SAFE mode. The software restart will re-initialize all hardware and software functions. To ensure that the sun pointing and the mission operability is achieved in the least time possible, the instrument rotation is not stopped, but it will be stopped in case of consecutive failures that triggers a software restart (Reconfiguration Module recovery escalation), or in case of a failure in the instrument itself or in one of the momentum compensation wheels. With the same philosophy, after the first restart, an attempt to enter the safe mode with the nominal configuration is performed. When another restart occurs without ground intervention, a full swap of the hardware to the redundant configuration is performed. The transition to the "ATT" phase of the SAFE mode will also be inhibited, in order to avoid possible issues on features common to the SAFE-ATT and the NOM mode such as reaction wheel commanding and gyro measurements. The B-DOT law used in SAFE-RATE can in fact guarantee the sun pointing using a reduced number of sensor and actuators with respect to SAFE-ATT (reaction wheel used only for momentum bias, gyro not used). The transient mode SAFE_MOM, entered in preparation of the SAFE mode, will use a different control loop with respect to the other modes using only momentum compensation wheels (only Z axis control), the gyro to estimate the rate and the uncompensated momentum and the sun sensors to perform sun pointing while the momentum is being compensated (it can take time if the instrument is being slowed down in an uncontrolled way after a failure).
During the controlled re-entry phase, the "RATE" phase of the SAFE mode will be inhibited below a certain perigee altitude (since MTBs torques are not enough to control the satellite at low altitude due to high drag torque). In case of software restart, the SAFE-ATT will be entered.

### 3.3 AOCS algorithms overview

A high-level overview of the AOCS algorithms inside the Guidance, Navigation, and Control (GNC) subsystem is reported in Figure 7.

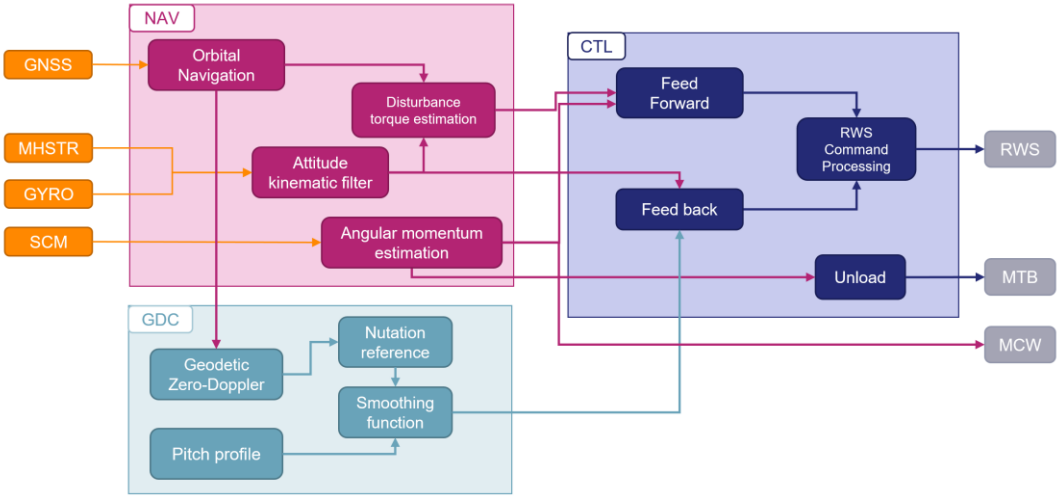


Figure 7. AOCS algorithms overview.

The AOCS algorithm and GNC subsystem work in a closed-loop manner, continuously measuring and adjusting the spacecraft's attitude and orbit based on the desired objectives and real-time sensor

feedback. They play a vital role in enabling precise pointing, stabilization, and maneuvering capabilities for spacecraft during their missions.
The navigation component of the AOCS algorithms utilizes data collected from star trackers and gyroscopes to estimate the spacecraft's current attitude and rate using techniques such as Kalman filtering or quaternion estimation. In addition to attitude estimation, the AOCS algorithms also incorporate orbital determination. GNSS data are used, along with orbital dynamics equations, to determine the spacecraft's position and velocity.

Position and velocity are used for guidance purposes. In detail, the guidance block is responsible for determining the reference attitude considering factors such as target destinations, orbital constraints, mission constrains and others.

The control component utilizes the guidance reference attitude and the navigation estimated attitude to calculate the attitude error and feed the controller. Control algorithms involve feedback control loops that continuously compare the desired state with the estimated state and adjust the control commands accordingly. These control commands are then sent to the spacecraft's actuators, such as reaction wheels, thrusters, or magnetic-torquers, to execute the required maneuvers.

# 4 CHALLENGES and CRITICAL SOLUTIONS

Given the spacecraft complexity, a few critical design solutions developed for CIMR are presented in more detail in this chapter.

## 4.1 Static and dynamic unbalances

The rotating instrument of CIMR satellite is responsible for static and dynamic unbalance effects, which contribute to the formation of nutation dynamics of the spacecraft and thus to the pointing performance. To mitigate these effects, a robust strategy based on the on-board estimation (at begin of life) of these unbalances through gyroscope rate measurements and ABS compensation has been developed.

The verification is based on a Monte Carlo Campaign over one-thousand runs and is summarized in Figure 8.

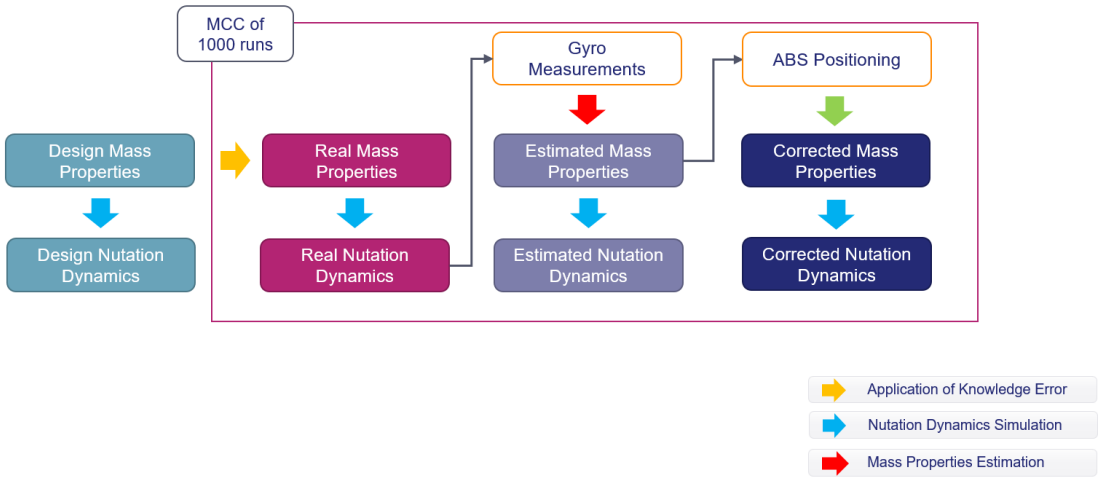


Figure 8. Verification process of the unbalance estimation algorithm.

For this purpose, CIMR satellite is supposed to be divided in two main bodies: body-1 identified with the platform and body-2 referred to the rotating part. For each run, the real mass properties (mass, center of mass and inertia matrix) are obtained by adding the relative knowledge errors to the default design mass properties. Then, the estimation process is tested on the real configuration and the ABS optimal masses position is computed in order to mitigate the nutation effect by changing the mass properties. The statistical distribution of the nutation amplitude for the corrected configuration describes the range of the disturbance that AOCS has to withstand during the mission.

Figure 9 shows the estimation algorithm that runs on-board at 8 Hz for a period of 1000 s inhibiting the actuation commands. The nutation over which the satellite undergoes is estimated on-board by gyroscope measurements (angular velocity) associated to the principal harmonic of the nutation. In detail, the scope of the algorithm is to find the body-2 center of mass offset ($c_{20x}$ and $c_{20y}$) and the product of inertia ($J_{20xz}$ and $J_{20yz}$ ).

Under the assumption that the SCM rotation angle ($\varphi$) and rotation rate ($\omega_s$) are perfectly known, the design mass properties model are loaded on the on-board software: $m_1$, $c_1$ and $J_1$ are the mass, center of mass and inertia of the body-1 (in MRF) and $m_2$, $c_{20}$ and $J_{20}$ are the mass properties of body-2 at default rotation angle $\varphi$=0 (in MRF).

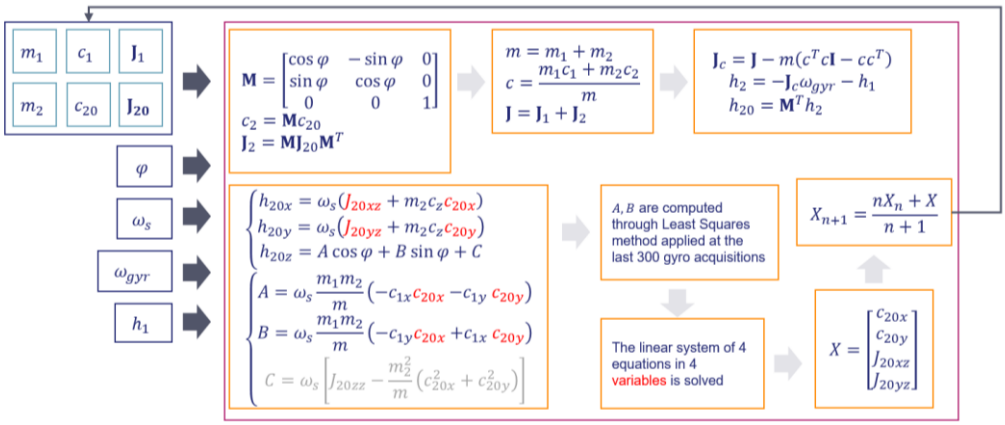

Figure 9. Estimation process.

Assuming that total spacecraft angular momentum is zero (no external disturbance torques) and that the internal angular momentum ($h_1$) due to the RWS and to the MCW is constant (during estimation process) and known, it is possible to calculate the internal angular momentum contribution ($h_2$) given by the rotating body-2.

The angular momentum profile $h_2$ is described as a constant vector on the XY plane if seen from the rotating reference frame ($h_{20}$), and as a sinusoid function of time (plus a bias) on Z-axis. This profile is thus fitted on the period with the Least Squares method applied to the last 300 gyro acquisitions. Then, a linear equation system is solved to find the unbalances parameters and, at the end, an averaging filter is applied to reduce the noise coming from the gyroscope and to ensure the convergence of the estimator.

Figure 10 reports one example run of the MCC where the blue line is the raw signal, the red one is the result of the averaging filter, and the dashed line is the real searched value. The constant phase at the begin is the initialization of the Least Square method buffer.

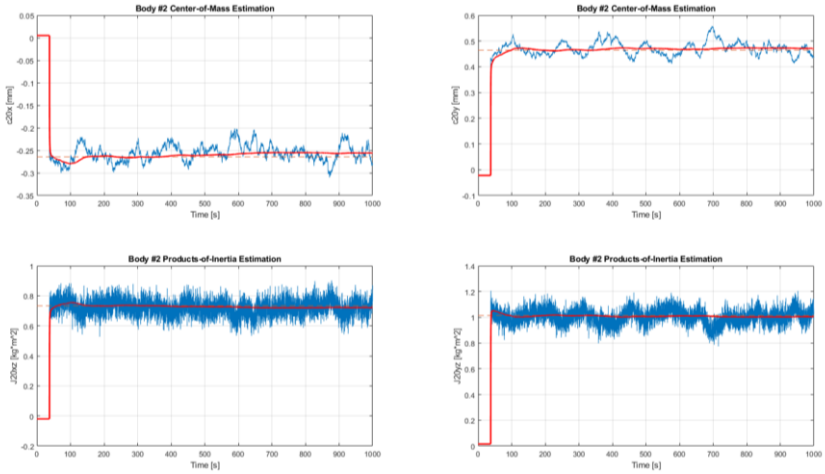


Figure 10. Center of mass and product of inertia estimation of the body2.

Together, Figure 11 shows the algorithm accuracy as the statistical distribution of the final error (after 1000 s) of all the MCC runs. With the current available data an accuracy of ~ 0.01 mm (1σ) on body-2 center of mass position and an accuracy of ~ 0.01 kg m$^2$ (1σ) for the body-2 products of inertia are reached. However, these are just preliminary results and have to be verified on the high-fidelity simulator.

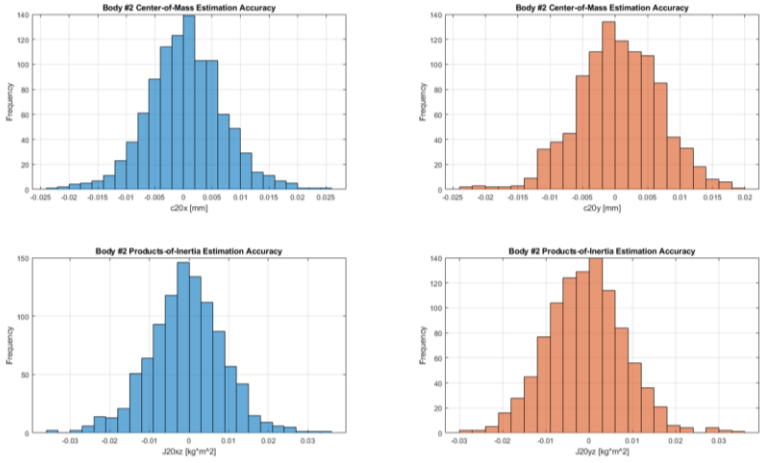


Figure 11. Body2 mass properties estimation accuracy through MCC.

Once the unbalances have been estimated, the three balancing masses ($m_{bk}$) on the body-2 are moved along Z-axis direction in order to minimize the nutation effect. Ideally, if body-2 transversal components of angular momentum ($h_{20x}$ and $h_{20y}$) were zeroed, the nutation amplitude would be null: this is the initial guess. In the linear equations system of Figure 12, the starred parameter identifies the mass properties after the correction. ABS is not able to change transversal components of center of mass position since the balancing masses move only along Z direction, meaning that only the product of inertia value can be affected. The third degree of freedom is used to impose that the longitudinal component of the assembly center of mass doesn't change after the correction by obtaining a solvable equation system.

$$\begin{cases} h_{20x} = \omega_s\left(J^*_{20xz} + m_2 c_{0z} c_{20x}\right) = 0 \\ h_{20y} = \omega_s\left(J^*_{20yz} + m_2 c_{0z} c_{20y}\right) = 0 \\ c^*_{0z} = c_{0z} \end{cases}$$

$$\begin{cases} \sum_{k=1}^{3} m_{bk}\, x_{bk} \Delta z_{bk} = J_{20xz} + c_{0z} c_{20x} \\ \sum_{k=1}^{3} m_{bk}\, y_{bk} \Delta z_{bk} = J_{20yz} + c_{0z} c_{20y} \\ \sum_{k=1}^{3} m_{bk}\, \Delta z_{bk} = 0 \end{cases}$$

Figure 12. Correction process.

### 4.2 Preliminary control design

The AOCS controller for the CIMR nominal mode has been synthesized, designed and tuned by following the logical process:

1. Construction of a linear flexible model of the spacecraft, obtained by linearizing the non-linear multibody flexible plant around an equilibrium point;
2. Design, synthesis and tuning of the controller on the plant of point 1.;
3. Robustness stability analysis of the nominal controller applied to the perturbed plant through Monte Carlo campaigns in the frequency domain;
4. Preliminary validation by time simulation on the plant of point 1.;
5. Final validation by Monte Carlo time simulation of the controller of point 2. applied to the non-linear multibody flexible plant.

The plant is built considering the rigid modes of the platform and different elastic sources. In particular, the flexible components are representative of the large inertia deployable antenna, the deployable solar array wings and the propellant sloshing elastic modes, whose effects are characterized by the presence of peaks in the frequency behavior of the plant. Indeed, Figure 13 reports the Bode diagram of the linearized plant, highlighting the contribution of each elastic component. In particular, the platform acts as double integrator, and red, light blue and dark blue markers represent the fuel sloshing, the deployable antenna and the solar array wings most significant flexible modes, respectively.

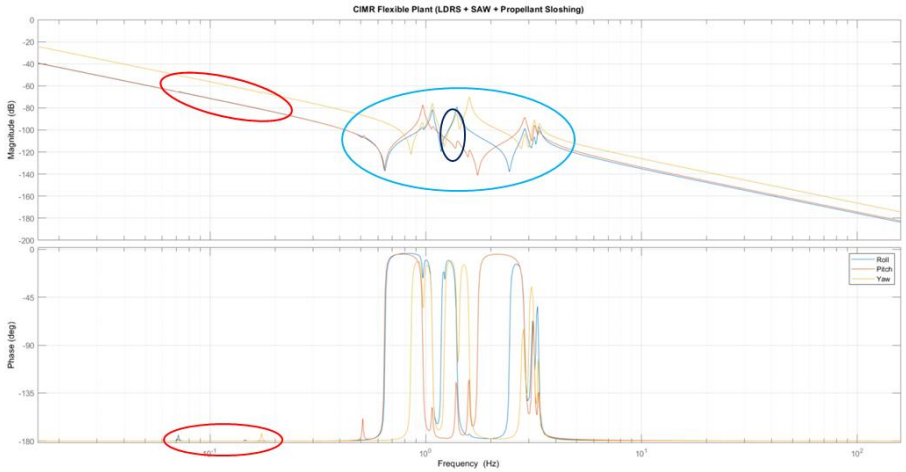


Figure 13. Bode diagram of the linearized flexible plant.

Due to the complexity of the structure, the plant stability is investigated.

Reference [6] reveals how instantaneous unstable modes may occur for some rotation angles of the payload. In case of CIMR, the plant stability is investigated by linearizing the model at each scan angle configuration and by perturbing the model parameters according with the available knowledge errors on the mass properties of the platform and of the flexible sources. In particular, a full rotation with a granularity of 1 degree is considered and, for each configuration, 50 runs are performed varying the mass properties. It brings to a MCC of 18.000 runs, whose results are reported in Figure 14 highlighting minimum, maximum and mean values for each of the 36 eigenvalues.
Indeed, each plant consists of 36 states and eigenvalues:

- The first six eigenvalues are associated to the rigid platform;
- Eigenvalues from 7 to 20 are associated to the rotating instrument elastic modes;
- Eigenvalues from 21 to 28 are associated to the solar array wings elastic modes;
- Eigenvalues from 29 to 36 are associated to the fuel sloshing elastic modes.

As a result, no unstable modes are found at any configuration, guaranteeing stability of the model delivered for control design.

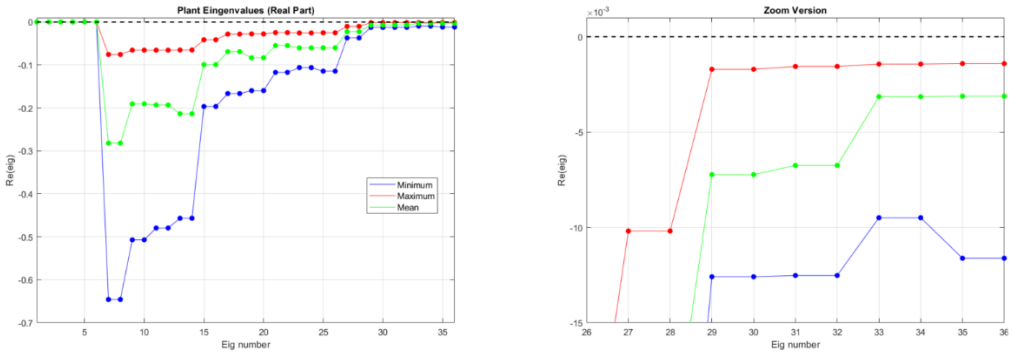


Figure 14. Minimum, maximum and mean value for each eigenvalue in a MCC of 18.000 runs.

Once the stability of the linearized plant for each scan angle is assessed, it is possible to design a control strategy to meet both the system stability and the pointing requirements.
To this purpose, a 3-axes decoupled controller based on a PID compensator augmented with a filtering chain is synthesized. Figure 15 illustrates the controller structure, where:

- the PID component handles the rigid body dynamics;
- the cascade of filters guarantees the system stability in terms of gain and phase margins.

To design the filters, both gain and phase stabilization techniques have been applied: first order lead and lag compensators shape the loop function guaranteeing phase and gain margins in order to satisfy the target ones, while second-order notch filters attenuate and, eventually, cut-off the highest resonance peaks at the most critical frequencies. To enforce stability with respect to disturbances and delays, critical gain and phase margins are set to 6 dB and 45 degrees, respectively.

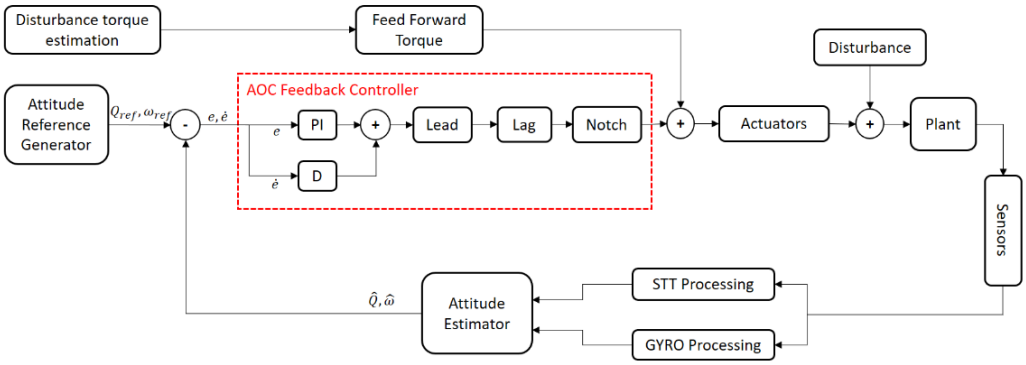


Figure 15. AOCS control scheme.

The tuning of the PID and the filters' parameters considers, in general, the best knowledge available about the system's mass properties and the modal frequencies of the most significant flexible modes. However, the presence of the large rotating antenna makes the total inertia seen by the platform to significantly change as a function of the scan angle. To account for this variation, it is chosen to compute values for the total inertia at different configurations of the scan mechanism and, then, take the mean value to scale the PID gains.

Figure 16 shows the Bode diagrams (single-axis for simplicity) of the filters used to shape the loop function. Here, the lead and lag compensators correct the phase to guarantee sufficient stability margins, and the notch filter, placed at the same frequency in which the resonance peak of the first structural mode of the rotating instrument has place, pushes down the gain attenuating the disturbance introduced by that elastic component. These filters are applied to each axis.

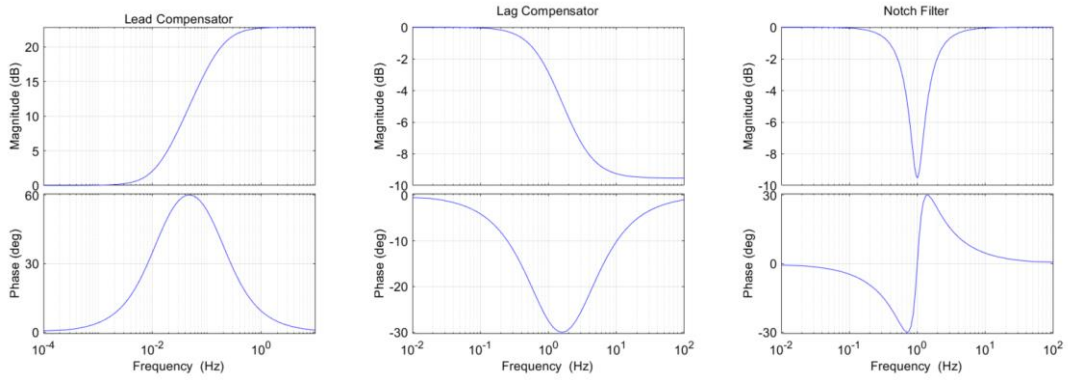


Figure 16. Single-axis lead, lag and notch filters.

Following, Figure 17 reports the frequency response of the open loop system together with the gain and phase margins of the controlled system, which result to be larger than the critical ones set previously.

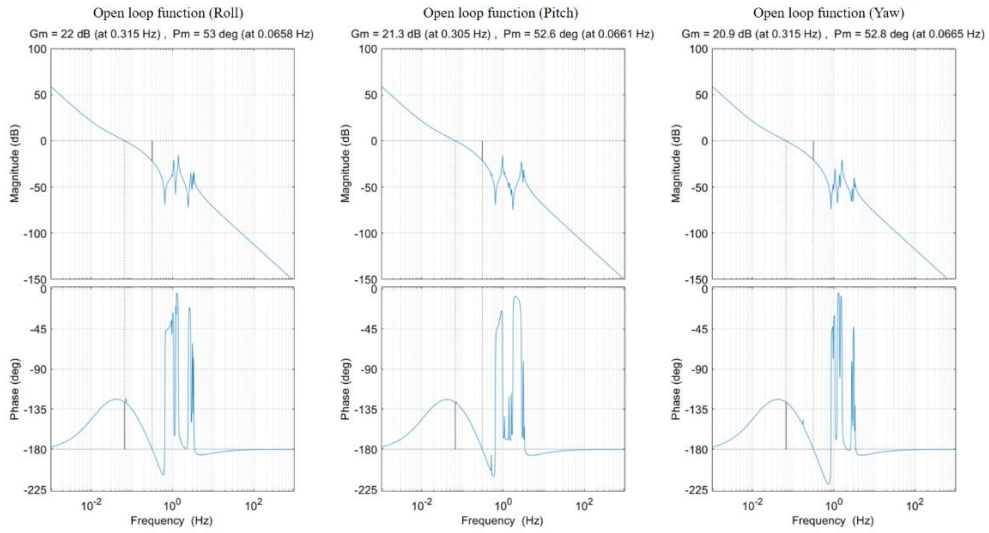


Figure 17. Frequency response of the open loop function.

Furthermore, the closed loop system behavior is investigated. In particular, Figure 18 reports the singular values of the Sensitivity (S) and Complementary Sensitivity (T) functions, highlighting how the flexible modes disturbances are attenuated by feedback.

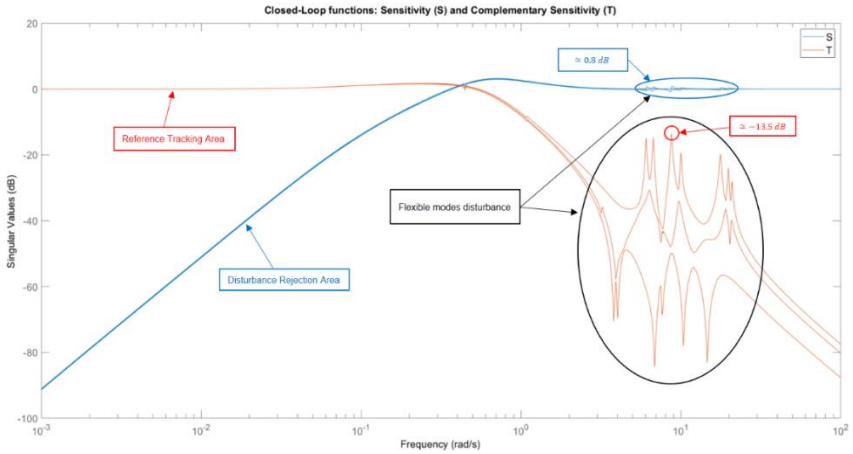


Figure 18. Sensitivity (S) and Complementary Sensitivity (T) functions.

Also, the presence of the scan mechanism controller regulating the instrument angular rate must be addressed. At this purpose, the scan mechanism control bandwidth introduces the main limit to the AOCS control one. Indeed, if the AOCS and the scan mechanism controller bandwidths result to be close from a frequency point of view, it would result in undesired coupling effects between the AOCS controller, the scan mechanism one and the lowest frequency flexible mode, potentially leading the closed loop system to instability. To avoid this kind of interaction, in the choice of the AOCS controller bandwidth, a sufficient amount of frequency separation must be considered with respect to the scan mechanism one.

It follows the closed loop performance is heavily dependent on the available knowledge of the system. Hence, a robustness analysis must be performed. To this purpose, because of the non-trivial identification of a worst case due to the complexity of the system, a Monte Carlo campaign is conducted in the frequency domain with the aim of analyzing the system stability. In this analysis, the nominal controller has been applied to the perturbed plant, obtained varying the scan angle, the mass properties of both platform and instrument, the modal frequencies and the modal damping of each elastic source according to the expected knowledge error. As a result, the controller was found to be robustly stable with respect to the selected range of uncertainties, guaranteeing both gain and phase margins larger than the critical ones and sufficient attenuation of the resonance peaks. Indeed, Figure 19 reports the gain and phase margins values over a Monte Carlo campaign of 3600 runs, together with their minimum, mean and maximum values, highlighting how both gain and phase margins never drop under the chosen critical values. Furthermore, the control bandwidth was preserved among all the runs, guaranteeing also the closed loop performance.

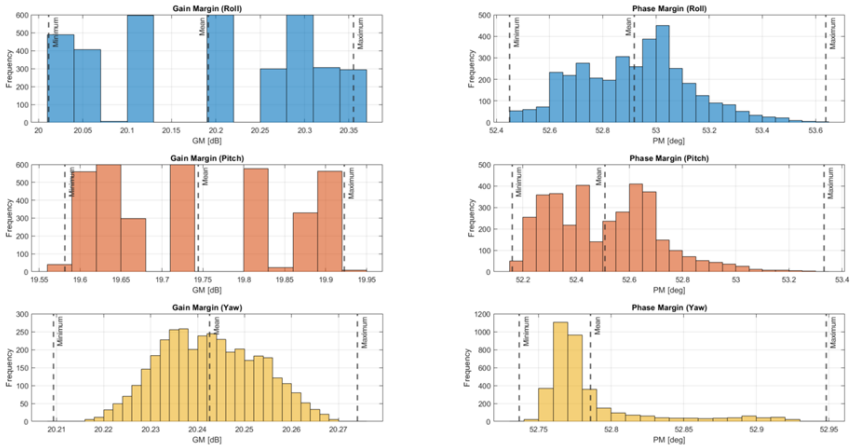


Figure 19. Gain and phase margins distribution.

### 4.3 Controlled re-entry manoeuver

CIMR re-entry phase consists of a series of controlled manoeuvers performed with several apogee retro-burn in order to lower the perigee altitude up to 50 km. These manoeuvers are complicated by two main factors: the aerodynamic drag effect and the thrust commanding, and are summarized in three main orbital phases:

- Apogee firing: the spacecraft performs high delta-v manoeuvers;
- Cruise: the spacecraft maintains the target attitude;
- Perigee critical drag: the spacecraft handles the high drag torque during perigee crossing.

The reference attitude applicable to the entire THRUST_REM mode has –Z axis toward velocity and the spacecraft +X axis close to nadir in order to have thrust force against inertial velocity vector. In addition, during this phase the instrument rotation is stopped.

The thrust control uses the four 20N thruster placed at the bottom of the platform, having each a tilt angle of 3 degrees with respect to the longitudinal axis of the satellite. Thruster commanding involves an adaptable partitioning of thrust, wherein a portion of the propulsive force is allocated to influence the re-entry trajectory, while the remaining thrust is employed to create a torque enabling precise attitude control.

During perigee lowering, especially below 200 km, the drag torque disturbance is no longer sustainable by AOCS actuators with nominal control performances. The strategy consists of implementing a robust technique in which the instrument is rotated to a constant position in order to minimize drag effects. Since the payload is off, AOCS has no pointing accuracy requirements to address: attitude controller feed-back gains are attenuated through a smooth switching function (using altitude as argument) to avoid reaction wheels angular momentum saturation. The same switch, represented in Figure 20, is implemented at the exit of drag phase, coming back to re-entry nominal control law, recovering attitude error in time for the next firing phase.

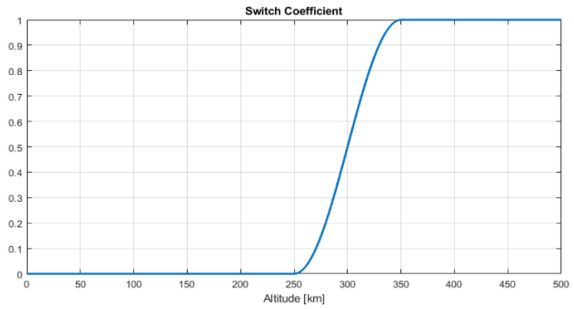


Figure 20. Switching function for the attitude controller

In this way it is possible to maintain the internal angular momentum always inside the RWS envelope at the worst case (one RW in failure). During this phase, the unloading of the RWS continues to be performed through MTB magnetic dipole as well as feed-forward of the control request.

Figure 21 represents the spacecraft drag torque, in which the peak corresponds to the attitude recovery at the exit of drag phase when the controller sees a high error. In particular, the maximum error that the controller detects is of about 8 degrees with respect to the nominal reference attitude (as shown in Figure 22).

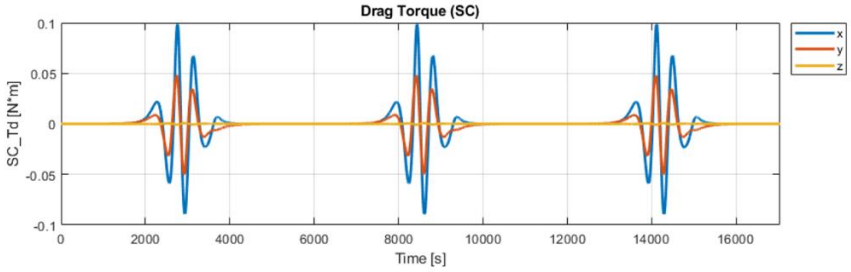


Figure 21. Drag torque.

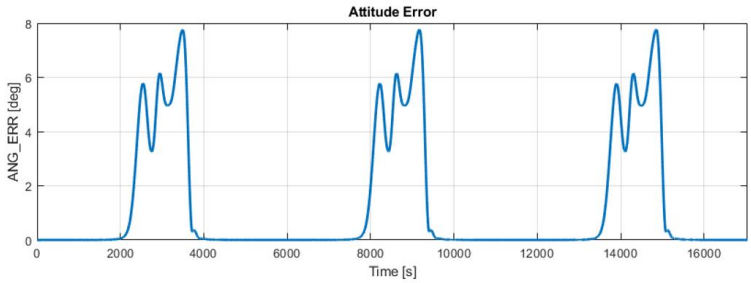


Figure 22. Platform dynamic stability: attitude error.

## 4.4 Propellant sloshing effect

Another important driver for the AOCS controller design is represented by the complex propellant sloshing dynamics that is the motion of the free surface of the fuel inside the partially filled tanks.

In the orbital environment, the microgravity load is comparable with the surface tension of the free surface of the propellant. The ratio between these two actions is given by the dimensionless Bond number $B_0$ defined by Eq.1:

$$B_0 = \frac{\rho g R_0^2}{\sigma} \tag{1}$$

where $\rho$ is the mass density of the propellant, $g$ is the main volume load acting on the propellant, $R_0$ is the characteristic dimension of the tank (most of the time it is the radius of the free propellant surface) and $\sigma$ is the surface tension acting on the meniscus of the fluid. In low-g regime, this number is small and the sloshing motion is really difficult to investigate. One possibility could be to simulate the whole coupled dynamics of the propellant in closed loop with the rigid multibody dynamics of the spacecraft by means of complex CFD analyses. However, due to high computational costs, this approach is suitable for validation rather than for design purposes. Typically, the sloshing effect is modelled by means of equivalent mechanical 2nd order models such as pendulums and, in case of small lateral excitations of the tanks, linear sprung-masses ([7]). The fundamental feature of such equivalent models is that they have to produce the same disturbing forces and torques on the tank walls as the real propellant dynamics. To this purpose, the parameters of the equivalent model such as the participating mass or the pendulum length are generally fitted with data acquired by means of experimental tests or numerical complex CFD simulations. Under some simplifying assumptions, the fundamental sloshing modes (natural frequencies and modal participation factors) can be accurately tuned by means of analytical formulations. In [8]-[9], these analytical models have been experimentally validated.

### 4.4.1 Assumptions

The assumptions underlying this analytical method are:

- Moderately low-g regime: $B_0 \in [1; 100]$;
- Small oscillations;
- Inviscid and incompressible fluid;
- Axisymmetric tanks.

Depending on the tank shape and size, the field Laplace equation deriving from the third hypothesis can be associated with different boundary conditions so that the solution can be approximated by means of modal decomposition techniques. It has been proven in [8] that the first mode is highly representative of the entire sloshing dynamics. This analytical solution provides the natural frequency of all the considered sloshing modes and the forces and torques exerted by the propellant on the tank walls as a function of the external excitation, the fill fraction and the Bond number.

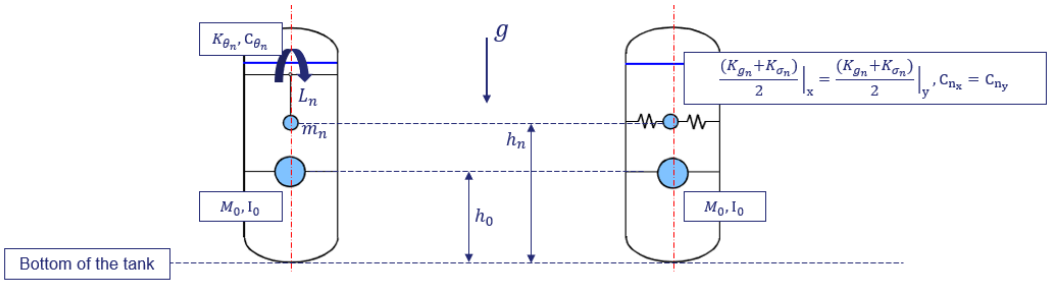


Figure 23. Equivalent mechanical models for linearized sloshing dynamics

### 4.4.2 Equivalent mechanical models and parameters tuning

As previously mentioned, the sloshing linearized dynamic equations can be described by the equivalent mechanical models depicted in Figure 23 in order to be included in the AOCS dynamic plant. Both models are characterized by a sloshing participating mass $m_n$, a fixed mass $M_0$ and an additional fictitious inertia moment $I_0$. In the pendulum model, the natural frequency of the n-th mode is governed by the length of the hinge $L_n$ and the hinge is also subjected to the action of a torsional spring of stiffness $k_{\theta_n}$ and damping $c_{\theta_n}$. Therefore, one can convert one model into the other by means of Eq.2 conversion formulae:

$$k_{g_n} = \frac{m_n g}{L_n} \qquad k_{\sigma_n} = \frac{k_{\theta n}}{L_n^2} \qquad c_n = 2\gamma_n m_n \omega_n \tag{2}$$

where the damping factor $\gamma_n$ governing the energy dissipation associated with the n-th mode is typically found via correlations of experimental data ([8]).

### 4.4.3 Analysis scenarios and main criticalities of the nominal operational mode

CIMR is equipped with a main cylindrical tank and two auxiliary spherical tanks. The sloshing natural frequencies and the corresponding modal participation factors have been derived for these three tanks in several scenarios involving different operational modes of the spacecraft (that cause different loads on the propellant) and at different stages of the operational lifetime of the mission (BOL, Mid-Life, EOL, disposal) which results in different fill fractions of the tanks. The participating mass fractions with respect of the total initial propellant mass (that is at BOL conditions) are shown in Figure 24 for all the considered scenarios.

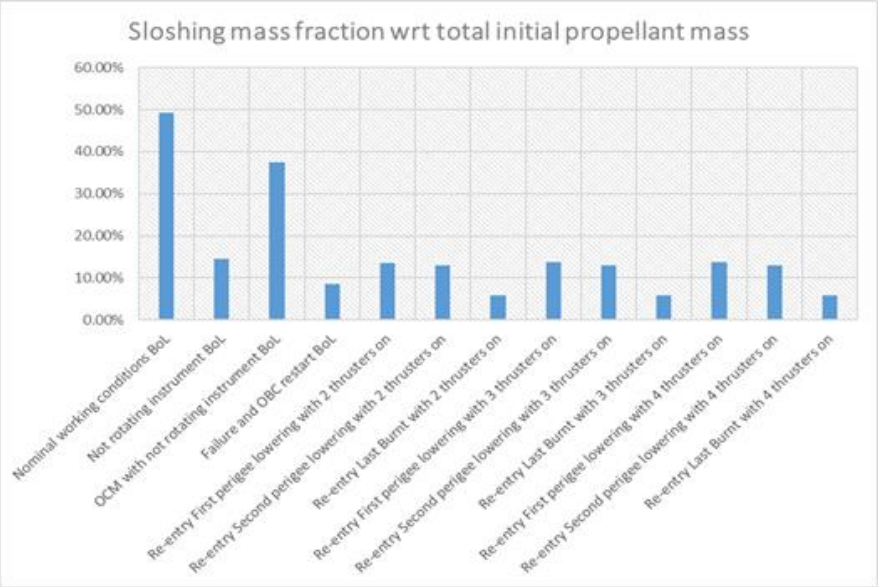

Figure 24. Participating propellant mass fractions for all the considered scenarios.

The nominal scenario is the most critical, not only because of the higher participating masses, but also because the "shaking" effect on the propellant, induced by the nutation dynamics of the platform, makes it rotates in the same direction of the payload. Therefore, for this case, the modal participation factors are provided with respect to a frame rotating together with the propellant and the fraction of the sloshing mass is also used to estimate the additional angular momentum contribution that has to be compensated by the MCWs according to the formula presented by Eq. 8.

$$H_{prop} = \left(\frac{m_s}{m_{tot}}\right) J_{zzC}^{tot}\, \omega_{SCM} + m_s\, r_{OC}^2\, \omega_{SCM} \tag{8}$$

In Eq.8, $m_s$ is the fundamental sloshing mass, $r_{OC}$ is the center of mass offset of the propellant with respect the tank symmetry line, $J_{zzC}^{tot}$ is the total propellant barycentric inertia moment about the rotation axis and $\omega_{SCM}$ is the angular rate of the instrument rotating part. Thus the estimated value of the additional angular momentum to be compensated in the worst case results in less than 5 Nms.

## 5 CONCLUSIONS

The design of the Attitude and Orbit Control system for the CIMR satellite presents several significant challenges that require careful consideration and innovative solutions. This paper has highlighted the most crucial and complex problems faced during the design and has proposed viable approaches to address them.

One of the key challenges was achieving precise attitude control and stabilization in the presence of external disturbances and uncertainties, primarily the mass properties of the large rotating antenna. To mitigate these effects, advanced control algorithm and sensor fusion techniques have been employed, enabling accurate determination and correction of the satellite's attitude. Furthermore, ensuring robustness and fault tolerance in the AOCS is crucial for mission success. Redundancy and fault detection mechanism have been integrated into the system, allowing for a quick identification

and mitigation of failures. This ensures the satellite can continue to function effectively even in the presence of unexpected events or anomalies.

## 6 REFERENCES


[1] website: https://www.esa.it/Applications/Observing_the_Earth/Copernicus/Copernicus_Sentinel_Expansion_missions.

[2] website: https://www.eeas.europa.eu/eeas/eu-arctic_en.

[3] ESA - Earth and Mission Science Division, *CIMR Mission Requirements Document (MRD)*, Official ESA Website, 2201 AZ Noordwijk, Netherlands, 11/02/2023.

[4] website: https://www.eoportal.org/satellite-missions/metop-sg#eop-quick-facts-section

[5] ESA – ESTEC, *CIMR Space Segment Requirement Document (SSRD)*, Official ESA Website, 2201 AZ Noordwijk, Netherlands, 28/10/2020.

[6] Oscar S. Alvarez-Salazar and Douglas Adams, *Pointing Architecture of SMAP's Large Spinning Antenna*, AIAA GNC Conference, August 19-22, 2013, Boston, MA.

[7] Dodge, F.,T.; "The New 'Dynamic Behaviour of Liquids in Moving Containers'"; Southwest Research Institute; San Antonio, Texas; 2000.

[8] Dodge, F.,T.; Garza, R., L.; "Experimental and Theoretical studies of Liquid Sloshing at Simulated Low Gravities", NASA report No.2; Southwest Research Institute; San Antonio, Texas; 1966.

[9] Dodge, F.,T.; Garza, R., L.; "Simulated Low-Gravity Sloshing in Spherical Tanks and Cylindrical Tanks with inverted Ellipsoidal Bottoms", NASA report No.6; Southwest Research Institute; San Antonio, Texas; 1968.